



Yan Wang, Fei Du, Georg R. Pesch, Jan Köser, Michael Baune, Jorg Thöming

Microparticle trajectories in a high-throughput channel for contact-free fractionation by dielectrophoresis

Journal Article as: peer-reviewed accepted version (Postprint)

DOI of this document* (secondary publication): <https://doi.org/10.26092/elib/2459>

Publication date of this document: 11/09/2023

* for better findability or for reliable citation

Recommended Citation (primary publication/Version of Record) incl. DOI:

Yan Wang, Fei Du, Georg R. Pesch, Jan Köser, Michael Baune, Jorg Thöming,
Microparticle trajectories in a high-throughput channel for contact-free fractionation by dielectrophoresis,
Chemical Engineering Science, Volume 153, 2016, Pages 34-44, ISSN 0009-2509,
<https://doi.org/10.1016/j.ces.2016.07.020>

Please note that the version of this document may differ from the final published version (Version of Record/primary publication) in terms of copy-editing, pagination, publication date and DOI. Please cite the version that you actually used. Before citing, you are also advised to check the publisher's website for any subsequent corrections or retractions (see also <https://retractionwatch.com/>).

This document is made available under a Creative Commons licence.

The license information is available online: <https://creativecommons.org/licenses/by-nc-nd/4.0/>

Take down policy

If you believe that this document or any material on this site infringes copyright, please contact publizieren@suub.uni-bremen.de with full details and we will remove access to the material.

Microparticle trajectories in a high-throughput channel for contact-free fractionation by dielectrophoresis

Yan Wang, Fei Du*, Georg R. Pesch, Jan Köser, Michael Baune, Jorg Thöming

UFT, Center for Environmental Research and Sustainable Technology, University of Bremen, Leobener Straße, D-28359 Bremen, Germany

HIGHLIGHTS

- A continuous, contact-free dielectrophoretic microparticle separator is proposed.
- Model predicting particle trajectory within the separator was experimentally validated.
- Theoretical fractionation resolution improves with increased voltage, reduced collector width and volume flow rate.
- High throughput can be achieved by trading-off design and operation parameters.

ARTICLE INFO

Article history:

Received 15 March 2016

Received in revised form

10 June 2016

Accepted 13 July 2016

Available online 15 July 2016

Keywords:

Fractionation

Dielectrophoresis

Particle trajectory

Resolution

High throughput

ABSTRACT

Continuous, contact-free fractionation of sensitive microparticles at high throughput is a challenge. For this purpose, we developed a sheath flow assisted dielectrophoretic (DEP) field-flow separator with a tailored arrangement of cylindrical interdigitated electrodes (cIDE) and observed size-dependent trajectories of dispersed particles. Using a voltage input of $200 V_{\text{eff}}$ at a frequency of 200 kHz, polystyrene particles (45, 25, and 11 μm in diameter) levitated to different heights along the channel length due to a negative DEP force. Experimental observations agree well with simulated particle trajectories that were obtained by a modified Lagrangian particle tracking model in combination with Laplace's and Navier-Stokes equations. By exploiting the size-dependent levitation height difference the desired particle size fraction can be collected at a specific channel length. The required channel length of the proposed cIDE separator increases with decreasing particle size to be separated. The quality of theoretical fractionation, which we quantify by resolution, improves strongly with reduced collector width, reduced volume flow rate and increased voltage input. The sensitivity of these dependencies increases with decreasing particle size. We calculated a theoretical throughput of up to 47 mL min^{-1} when trading-off design and operation parameters, allowing for contact-free fractionation of sensitive microparticles with negligible shear stress.

1. Introduction

Separation of microparticles is a widespread requirement for pharmaceutical production and in biotechnology, diagnostics and analytics (Jin et al., 2014; Lenshof and Laurell, 2010; Yamada et al., 2004); even the generation of several fractions is often required (Fedotov et al., 2011; Messaud et al., 2009). Fractionation techniques, such as differential centrifugation, membrane filtration, field-flow fractionation and capillary electrophoresis are well established, especially in analytics. All these techniques, however, are limited in throughput and might dominate total production costs if large volumes of dispersions have to be processed. While

centrifugation is labour intensive and exposure to a high acceleration might cause damage to shear-sensitive biological products (Fukuda and Schmid-Schönbein, 2002; Xie et al., 2010), membrane filtration often suffers from membrane fouling (Fedotov et al., 2011; Seminario et al., 2002). Field-flow fractionation requires a ribbon-like channel of rigorous dimensions that allows extremely short relaxation time for particles to reach their equilibrium and adequate retention time differences between particles for effective elution (Messaud et al., 2009). In addition, the lack of an external force for sensitivity control of the particles' position results in a limited selectivity (Huang et al., 1997). Capillary electrophoresis depends on differences in particles' electrophoretic mobilities and is thus restricted to charged particles. Besides, the utilization of a capillary as separation channel confines the system to a low throughput of maximum $1 \mu\text{L min}^{-1}$ that makes it suitable solely for sample analysis and detection (Han et al., 2015; Katasonova

* Corresponding author.

E-mail address: feidu@uni-bremen.de (F. Du).

and Fedotov, 2009). Some other methods such as hydrophoresis (Song and Choi, 2013) and inertial microfluidics (Kuntaegowdanahalli et al., 2009) have also been used for contact-free fractionation of particles but they have their own drawbacks. Recently, Zhang et al. (2014) reported an inertia based particle separation approach by employing a serpentine channel for continuous separation of particles based on size (Stokes number) at flow rates reaching 0.7 mL min^{-1} . It was, however, impossible to determine the specific particle size threshold, as the forces that act on particles could not be adjusted.

Among various separation approaches, a promising technique is dielectrophoretic fractionation that relies on differences in particle size (Chuang et al., 2014; Han et al., 2009; Kralj et al., 2006; Park and Jung, 2009) and/or electric properties (Doh and Cho, 2005; Huang et al., 1997; Li et al., 2007; Wang et al., 1998). Dielectrophoresis (DEP) is an electrokinetic technique that can be used to manipulate the motion of both charged and neutral particles. DEP movement is caused by dielectric polarization of matter in inhomogeneous electric fields and by the resulting macroscopic electric forces (Morgan and Green, 2003). Both magnitude and direction of the DEP force depend on the relative polarizability of the particles in the suspending medium. Particles being more (less) polarizable than the surrounding medium will move towards stronger (weaker) electric field regions, termed as positive (negative) DEP. Dielectrophoretic motion is driven by the spatial change of the electric field, i.e. gradient of the square of the electric field, and depends on the volume of the particle as well as the electric properties of both the particle and the suspending medium. Due to demonstrated simplicity, high sensitivity and selectivity, DEP is considered to be a very effective approach for particle separation (Khoshmanesh et al., 2011; Pethig, 2010, 2013; Voldman, 2006).

Up to now, the majority of DEP research is still concentrated on lab-on-a-chip scale setups with throughputs being typically in the $\mu\text{L min}^{-1}$ range (Bisceglia et al., 2015; Cheng et al., 2009; Lee et al., 2013; Li et al., 2010; Ling et al., 2012). DEP separation of particles or cells with relatively high throughput to reach clinical and industrial scale has rarely been reported. Çetin and Li (2011) pointed out that, in order to make DEP-based systems competitive with conventional separators, research is required on the improvement of their throughput. Although some researchers have made progress on increasing the flow rate of DEP-based devices, it remains an ongoing problem. Čemažar et al. (2016) designed a high-throughput contactless DEP device that uses cell-size pillars to isolate and enrich rare cell samples. The proposed device has the capability of separating cells with a high flow rate of $37 \mu\text{L min}^{-1}$ and throughput of a few million cells per hour while maintaining high cell viability. Indeed, the viability of cells is a major concern in DEP bioparticle manipulation since both the electric field strength and the Joule heating are known to directly affect cells (Qian et al., 2014). Gadish and Voldman (2006) proposed a dielectrophoretic microfluidic device for concentrating particles with high throughput of up to $100 \mu\text{L min}^{-1}$, which served as an interface between preparative sample collectors and microscale detectors. Moon et al. (2011) reported a novel method for continuous separation of circulating tumor cells from blood cells by combining multi-orifice flow fractionation and DEP. They achieved a high separation efficiency at a flow rate of $162 \mu\text{L min}^{-1}$, indicating the possibility for high-throughput application for clinical cell sorting. Markx et al. (1994) used AC DEP to separate viable and non-viable yeast cells with a volumetric flow rates of $500 \mu\text{L min}^{-1}$. Wang et al. (1998) introduced dielectrophoretic field-flow fractionation (DEP-FFF) for separating two types of polystyrene beads with different surface functionalization. The degree of separation, characterized by the ratio of the elution peak times of two populations, was not compromised even at high flow rate of 1000μ

L min^{-1} . Pesch et al. (2014) presented a novel method to recover submicron particles by using a high-throughput dielectrophoretic switchable filtration. Good separation and recovery efficiencies of nanocapsules were achieved in semi-continuous operation at a flow rate of 1 mL min^{-1} . Baune et al. (2008) experimentally investigated DEP systems with electrode distances in millimeter-scale, which presented the prospect of scaling-up DEP application in separation technology. Later, Du et al. (2008) followed the same approach by developing a DEP particle separator for fractionating gold particles from an aqueous suspension of heavy minerals with a high throughput of 141 mL min^{-1} . This throughput is, to the best of our knowledge, the highest one reported in literature so far and the only one showing potential for DEP application in production scale. It is, however, so far limited to discontinuous operation. Kang et al. (2009) identified the required trade-off between high throughput and high separation efficiency at continuous operation and proposed a microfluidic device using embedded electrodes and an insulating obstacle for continuously separating $5 \mu\text{m}$ and $10 \mu\text{m}$ particles.

Generally, a high throughput could be achieved by scaling up the dimensions of the DEP separator. The major problem is, however, the conflict between the dimensions of the electrode configuration and suspension flow rate as well as the voltage input for efficient particle movement. As an example, for enhancing the suspension flow rate at a given DEP force acting on a particle, an increase of both characteristic length (i.e., the distance between electrodes) and voltage is required to maintain the same efficiency. On the one hand, a DEP system with low voltage input requires a very small characteristic length to generate sufficient electric fields that could hardly be realized in case of high flow rates. On the other hand, a DEP system based on a high voltage and a large characteristic length inevitably requires accordingly high energy input, which in turn causes relatively large resistive loss of energy and undesired side effect, such as Joule heating (Du et al., 2007; Ramos et al., 1998; Wang et al., 2014, 2015; Wood et al., 2013). Therefore, a tailored design of the electrode arrangement for providing appropriate DEP force on particles is required to solve the abovementioned problems in DEP scale-up and to realize maximized separation efficiency at minimized energy demand.

With respect to the electrode arrangement, the interdigitated electrode (IDE) structure is the most commonly used electrode configuration in DEP applications. In particular, the independence of the channel height on the space between electrodes of such an array gives the opportunity to scale up the DEP separation channel. Wang et al. (2014) reported that cylindrical IDE (cIDE) configurations provide more homogeneously distributed gradient of the square of the electric field near the electrodes compared to the traditional plate IDE configuration. The homogeneously distributed gradient of the square of the electric field in a cIDE-DEP system results in a more effective and sustained DEP force field for particle manipulation.

Wang et al. (2015) subsequently discussed a tailored design of such cIDE structures. The dependence of the gradient of square of the electric field distribution on its structure parameter, i.e., the space between electrodes L , was numerically investigated and experimentally evaluated. The results showed that DEP systems, in which the electrode spacing exceeds the electrode diameter, provide a comparably smaller DEP force close to the electrode surface, while simultaneously the effective DEP working range, i.e., possible channel size, is enlarged. This lays the foundation for designing a high-throughput DEP based device.

In this work, we propose a continuous cIDE-DEP separator for contact-free size-based microparticle fractionation. A combined model based on a modified Lagrangian particle tracking solver that calculates the force fields according to Laplace's equation and the Navier-Stokes equation was validated experimentally by

measuring motion trajectories of polystyrene microparticles (45, 25, and 11 μm in diameter) in a fluid flow and electric field of a tailored cIDE separator. Using this as a basis, we conducted a numerical study to evaluate the fractionation performance as a function of operation and design parameters.

2. Materials and methods

2.1. Layout of the cIDE separator

The proposed cIDE-DEP separator (Fig. 1a) consists of two inlet channels (left), a particle separation channel (middle) and an outlet channel (right). The two inlet channels are a 2 mm wide suspension flow inlet and a 5 mm wide sheath flow inlet with 45° deflection in between. The design of the sheath flow channel is based on the idea of maximizing the initial DEP force by driving the particle motion as close as possible to the surface of the first electrode, where the electric field gradient is highest. The separation channel consists of an interdigitated array of 2 mm diameter cylindrical electrodes. The electrodes generate a highly inhomogeneous electric field with maximum field strength very close to the electrodes. Particles experiencing negative DEP will therefore be repelled from the electrode. The first four electrodes are arranged with increasing distance between them, i.e., 1 mm, 1.5 mm and 2 mm. All other electrodes have a constant 2 mm tip-to-tip distance. The collector at the end of the separator is

subdivided into n single collector channels (Fig. 1c). Each collector channel is utilized for collecting particles of certain size fraction (e.g. d_p^* , d_{p1}^* and d_{p2}^*) (Fig. 1d). For the separator a channel height H of 5 mm was chosen, which presents a good trade-off between channel height and low disturbance of the DEP induced particle motion by Joule heating (Wang et al., 2015).

The particles that are injected at the top position of the suspension inlet are forced by the sheath flow towards the channel bottom. Consequently, they enter the separation channel at the bottommost position very close to the surface of the first electrode, where the DEP force is the strongest. The narrowest spacing between the first pair of electrodes can generate the strongest DEP force in the vicinity of them, allowing a fast levitation due to the negative DEP effect (Wang et al., 2015).

With increasing height above the electrodes, both the field strength and the field gradient are decreasing. Particles experiencing negative DEP should be levitated depending on their diameter. It can be expected that the resulting difference in levitation height is remarkable due to the cubic dependence of the DEP force on the particle diameter. Controlled by the diameter, particles will reach their final equilibrium height (at which the DEP force matches the gravitational body force) at a different time (Mathew et al., 2015). A size dependent separation can be achieved only during the transient state before this equilibrium is reached. It is important to distinguish the proposed fractionation method from DEP-FFF, in which particles are fractionated according to their dielectric properties at equilibrium conditions (Huang et al., 1997;

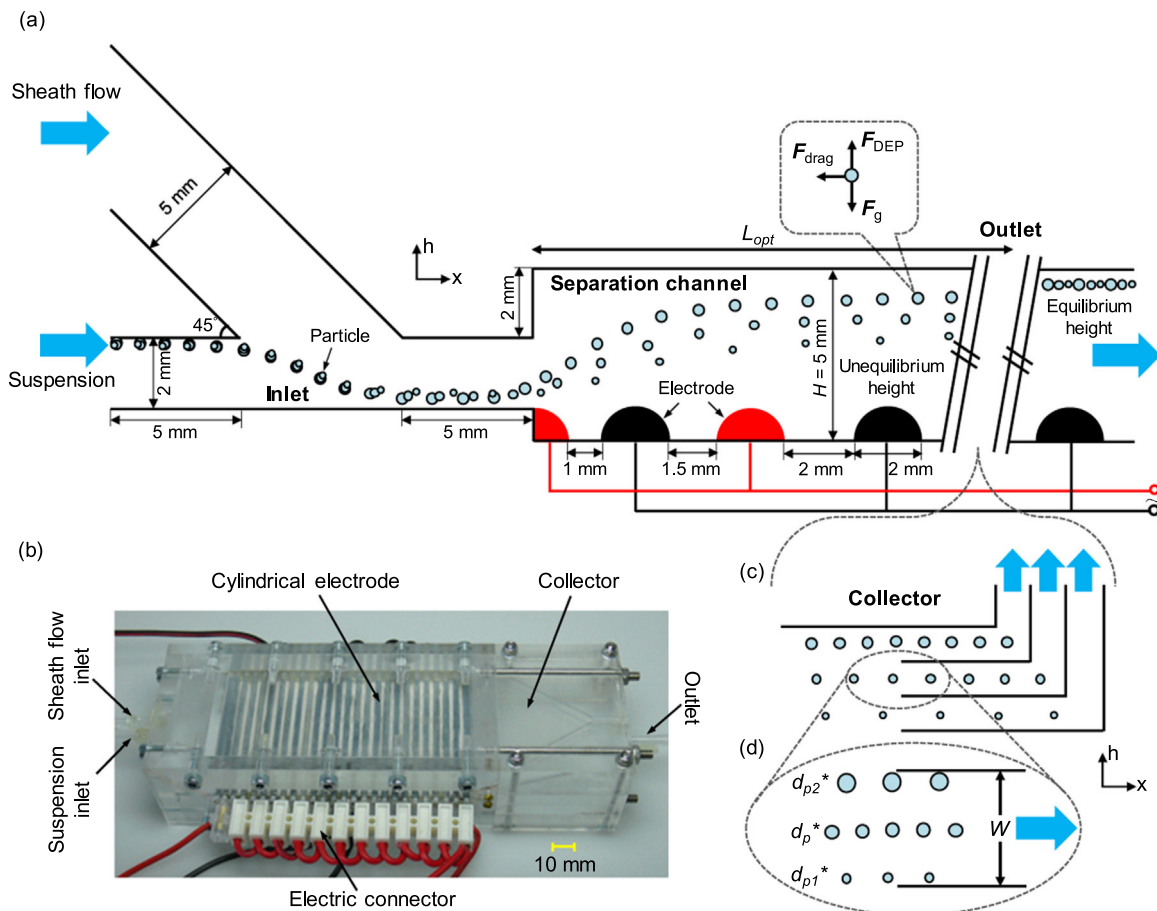


Fig. 1. (a) Two-dimensional schematic diagram (side view) of cIDE-DEP separator of channel height H and hydrodynamic particle motion trajectories. Gravity points from top to bottom; (b) Experimental setup of the cIDE-DEP separator composed of 26 cylindrical electrodes with diameter of 2 mm and electrode length of 50 mm; (c) Schematic representation (part view) of the particle collector. Particle trajectories determine optimal channel length L_{opt} , at which the collector (comprising n single collector channels of width $W=H/n$) is best positioned; (d) Single collector used for obtaining the target fraction with mean particle size d_p^* . The resolution is determined by the smallest particle size (d_{p1}^*) and the biggest particle size (d_{p2}^*) entering the single collector channel.

Leu and Weng, 2009; Wang et al., 1998). Hence, the latter electrodes are spaced wider to provide a larger DEP working area, insuring sustainable and effective DEP particle levitation throughout the whole separation process (Wang et al., 2015).

2.2. Numerical simulation

2.2.1. Particle motion analysis

Particle motion trajectories within the cIDE separator were predicted by implementing a modified Lagrangian particle tracking code (Kang et al., 2006) in *OpenFOAM* using the following simplifications:

1. The influences of the particles on both fluid flow and electrical field were neglected, since the particles are much smaller than the electrode spacing (Kang et al., 2006).
2. The effect of Brownian motion was ignored, as particles are larger than 1 μm (Kissa, 1999).
3. Electrostatic and dielectrophoretic interactions between particles are not considered due to the low input suspension concentration (chosen to enable observation of single particle motion trajectories).
4. Wall effects are negligible with the assumption that particles are always far from either side of the channel wall.
5. Any thermal effect induced by Joule heating on both particles and fluid medium is not considered due to the negligible temperature rise of ΔT below 0.5 K (estimation see Appendix A1).

Therefore, the motion of particles is controlled only by a negative DEP force (F_{DEP}), a hydrodynamic drag force (F_{drag}) and a gravitational body force (F_g), as illustrated in Fig. 1a.

In the simple point-dipole approach, the DEP force is determined by the gradient of the square of the electric field generated by the applied electrode configuration. In the case of linear and isotropic dielectrics, the force on a spherical particle with radius a suspended in a medium with relative permittivity ϵ_m can be written as (Pohl, 1978):

$$F_{\text{DEP}} = 2\pi a^3 \epsilon_0 \epsilon_m \text{Re}[\tilde{K}] \nabla |E|^2 \quad (1)$$

where $\epsilon_0 = 8.854 \times 10^{-12} \text{ F m}^{-1}$ is the permittivity of free space, E is the electric field, and $\text{Re}[\tilde{K}]$ is real part of the Clausius–Mossotti factor, a parameter defining the effective dielectric polarizability of the particle in the medium. The $\text{Re}[\tilde{K}]$ depends upon the dielectric properties of both particle and medium and is given as (Jones, 1995):

$$\text{Re}[\tilde{K}] = \text{Re}\left(\frac{\tilde{\epsilon}_p - \tilde{\epsilon}_m}{\tilde{\epsilon}_p + 2\tilde{\epsilon}_m}\right) \quad (2)$$

where subscripts p and m represent the particle and the medium, respectively, and $\tilde{\epsilon} = \epsilon - \frac{j\sigma}{\omega}$ is the complex permittivity, with the conductivity σ , the angular frequency ω ($\omega = 2\pi f$, where f is frequency of electric field) and the imaginary unit $j = \sqrt{-1}$. Depending on the sign of $\text{Re}[\tilde{K}]$, the particle will either show positive DEP (p-DEP, $\text{Re}[\tilde{K}] > 0$) or negative DEP (n-DEP, $\text{Re}[\tilde{K}] < 0$) and hence will either move towards stronger or weaker electric field regions. We note that Eq. (1) is only valid for spherical particles and in case the particles are much smaller than the spatial change of the electric field (Nili et al., 2011).

With the presence of fluid flow, a hydrodynamic drag force acts on the spherical particles. At laminar flow with low particle Reynolds number ($Re_p < 0.1$), which is known as Stokes drag (Leal, 2007), the force is given as:

$$F_{\text{drag}} = 6\pi\mu_m a(u_m - u_p) \quad (3)$$

where μ_m is dynamic viscosity of the fluid medium and u_m and u_p are the velocities of the fluid medium and the particle, respectively.

For a spherical particle with mass density ρ_p , suspended in a fluid medium with mass density ρ_m , a gravitational force arises due to the density difference:

$$F_g = \frac{4}{3}\pi a^3 (\rho_m - \rho_p)g \quad (4)$$

where g is the gravitational acceleration.

Three forces are acting on the particle in the separation channel, i.e., gravity, hydrodynamic drag and DEP. Since the time scale of particle acceleration is much smaller than the residence time, we can neglect inertia and assume that the particle velocity is only a function of the spatial position. The force balance is then given in vector notation by:

$$F_{\text{DEP}} + F_{\text{drag}} + F_g = 0 \quad (5)$$

The force field acting on a particle with known properties is given in the entire separator domain. The velocity u_p and the trajectory of a particle can thus be easily obtained by employing a suitable tracking algorithm and by solving Eq. (5).

Since the DEP force decreases with height above the electrodes, the particles will eventually reach a steady equilibrium levitation height, at which the DEP force balances with gravity and the vertical component of F_{drag} in Eq. (5) is zero. This height is independent of particle size if equilibrium is reached (Markx et al., 1997; Mathew et al., 2015) while the time for particles to ascend and reach their equilibrium height is size dependent and usually takes several minutes. For the 45 μm particle in our case study, by applying with voltage input of 200 V_{eff} at frequency of 200 kHz and volume flow rate of 4.7 mL min^{-1} , it takes about 3 min from entering the separation channel ($h = 1.3 \text{ mm}$) to reaching the final equilibrium height ($h = 4.5 \text{ mm}$). Due to the cubic dependence of the DEP force on the particle radius a , particles will ascend at different velocities depending on their size before reaching the equilibrium height, i.e., bigger particles will ascend with higher velocities than smaller particles. Eventually, fractionation can be achieved by extracting the particles during their transient ascend before the equilibrium is reached.

2.2.2. Electric field and flow field calculation

The electric field can be determined by solving Laplace's equation for the electric potential ϕ (Castellanos et al., 2003):

$$\nabla^2 \phi = 0 \quad (6)$$

The value of the gradient of square of the electric field ($\nabla |E|^2$) can be evaluated as a function of ϕ (Wang et al., 2014). *OpenFOAM* was used to calculate the distribution of $\nabla |E|^2$ within the DEP separation channel. The simulation domain was considered to be two-dimensional since the electrodes are long compared to their diameter (Green et al., 2002). *Dirichlet* boundary conditions ($\phi = \pm U_{\text{rms}}$) where applied at the electrode surface to match the AC input signal (Crews et al., 2007). *Neumann* boundary conditions ($\frac{\partial \phi}{\partial n} = 0$) where applied at the channel inlets and the channel wall (Lewpiriyawong et al., 2010). A *cyclic* boundary condition was applied at the right side for simulating the presence of an arbitrary number of electrodes (Cao et al., 2008).

The flow field of an incompressible, Newtonian fluid is calculated by solving the Navier–Stokes equation together with the continuity equation (Çetin et al., 2009):

$$\nabla \cdot u_m = 0 \quad (7)$$

$$\rho_m(u_m \cdot \nabla)u_m = -\nabla p + \mu_m \nabla^2 u_m \quad (8)$$

where p is the pressure. Non-slip velocity boundary conditions were assigned on the channel wall and each electrode, whereas uniform values of velocity were specified at both channel inlets corresponding to the experimental volumetric flow rates of the fluid.

To ensure stable solutions of both fields calculation, the dependence of the field distribution on mesh resolution was evaluated in the computational domain (see [Appendix A7](#)).

2.3. Experimental setup

The setup included a CCD camera (DFK 31AU03, Imaging source co. Ltd), a confocal tele-lens, a function generator (HM8131-2), a power amplifier (FM1290), a peristaltic pump (MS-216), a syringe pump (Legato 270), a cooling system and a cIDE-DEP cross-flow channel ([Fig. 1b](#)) equipped with cylindrical IDEs. Conventional mechanical processes such as precision milling were utilized for fabrication of the millimeter scale device and for controlling the distance between electrodes. Electrodes were made of titanium insulated by rutile for diminishing problems in conductive aqueous media such as the risk of short circuit and electrochemical reaction. The cooling system composed of two Peltier elements (input 12 V, 10 A, controlled by a Peltier controller with an NTC thermal sensor) was mounted under the electrodes to dissipate any heat generated by the current. Non-functionalized polystyrene microsphere (PS) particles (Polysciences, Inc., $\epsilon_p=2.55$, $\rho_p=1005 \text{ kg m}^{-3}$) with diameters of 45 μm , 25 μm , and 11 μm were utilized in the experiment.

The original microparticle suspensions contain slight anionic surface charge and minimal surfactants during manufacturing process and the final preparation as indicated by the particles provider. To keep a minimized impact of the surface charge on particles' DEP effect, all the experimental particles were pretreated. Two steps of pretreatment were conducted: particles were washed three times with 0.1 mol L⁻¹ sodium chloride solution for removing residual surfactants and thereby reducing their surface charges ([Bettelheim et al., 2012](#)); afterwards, these particles were rewashed three times with Milli-Q water. After the pretreatment, the particles were resuspended in Milli-Q water and tested in a batch DEP setup mounted with IDE electrodes. All pretreated particles presented strong n-DEP effect.

For examining the effectiveness of pretreatment, zeta potential of three different sized particles were measured using a Beckman Coulter DelsaTMNano C (Beckman Coulter, Krefeld, Germany) that features a diode laser (30 mW, $\lambda_0=658 \text{ nm}$). The zeta potential measurements were carried at scattering angle 15° and the scattered light was detected using a photo multiplier tube and analyzed with a digital correlator. A sample volume of 5 mL was filled in a Flow Cell and equilibrated at $T=298.15 \text{ K}$ for 1 min before the measurement time of $3 \times 140 \text{ s}$. The correlation function is recorded at 5 positions in the flow channel to correct for the electroosmotic flow profile. For the evaluation the Smoluchowsky equation and the properties of pure water were used (refractive indices $n(658 \text{ nm}, 298.15 \text{ K})=1.3328$, $\mu_m(298.15 \text{ K})=0.8878 \text{ cP}$, $\epsilon_m=78.3$ as given by the Beckman Coulter software). Measurement was considered valid in case the mobility profile gave a parabolic shape expected from electrophoretic light scattering theory ([Xu, 2001](#)).

The conductivities of the pretreated particles was evaluated thereafter using double layer conductance approximation ([Ermolina and Morgan, 2005](#)) as $\sigma_p(45 \mu\text{m})=2.4 \times 10^{-7} \text{ S m}^{-1}$, $\sigma_p(25 \mu\text{m})=1.6 \times 10^{-5} \text{ S m}^{-1}$ and $\sigma_p(11 \mu\text{m})=2.1 \times 10^{-5} \text{ S m}^{-1}$, respectively (for detailed calculations see [Appendix A3](#)). The zeta potential of the particles was decreased (or stayed constant in case of 11 μm particles) after washing with sodium chloride solution,

which indicates a partial surface charge removal due to the washing step (see [Appendix A2](#) for the particles' zeta potential data). According to Eq. (2), the particles' DEP response depends on the interplay between frequency, conductivity and permittivity of the particles and the medium. Due to their double layer conductance, even after washing the particles have a comparably high overall conductivity, which is, for 11 μm and 25 μm , higher than that of the Milli-Q water used as suspension (Milli-Q[®] water, $\sigma_m=5.5 \times 10^{-6} \text{ S m}^{-1}$, $\epsilon_m=78.5$, $\rho_m=1000 \text{ kg m}^{-3}$). This is quite usual for polystyrene particles ([Ermolina and Morgan, 2005](#)). The 11 μm and 25 μm particles should therefore present positive DEP at low frequencies and negative DEP at high frequencies (due to the much lower permittivity of polystyrene compared to the suspending medium). The 45 μm particle should show negative DEP at all frequencies (as both conductivity and permittivity are lower for PS than for Milli-Q water). According to Eq. (2) and to the results of preliminary experiments, all three particle sizes show negative DEP at the utilized frequency of 200 kHz (see [Appendix A4](#) for the dependency of $Re[\tilde{K}]$ on the field frequency). The real part of Clausius-Mossotti factor $Re[\tilde{K}]$ for three different size particles at this frequency was calculated using Eq. (2) to be the identical value of -0.48 .

A syringe pump and a peristaltic pump were employed for introducing suspension and sheath flow at flow rates identical to those used in simulation, respectively. The input voltage was 200 V_{eff} with an electric field frequency of 200 kHz. The optical system consisting of a CCD camera equipped with a telelens was applied to observe and record the particle motion trajectories in the region of the first pair of electrodes. The particle trajectories were recorded as a digital video clip and processed using *Sigmascan Pro 5.0* by defining particle positions (x, h) on every picture extracted at each 1/30 s. Both the horizontal position x and the height of particle h were determined by comparing to the reference objects included in each picture. To minimize the experimental error, trajectories of ten individual particles of the same size were recorded and averaged.

3. Results and discussion

3.1. Simulation of the $\nabla|E|^2$ distribution

The calculated $\nabla|E|^2$ distribution within the DEP separation channel shows that the highest value of the $\nabla|E|^2$ is found at both sides of the electrodes where the distance between the electrodes is closest ([Fig. 2a](#)). With increasing height above the electrodes, the $\nabla|E|^2$ value decreases. As expected, electrodes with closer spacing, i.e., the first pair electrodes on the left side with 1 mm space in between, generate higher $\nabla|E|^2$ at positions very close to the electrode surface compared to those with 1.5 mm and 2 mm spacing. In particular, the maximum $\nabla|E|^2$ and thus strongest DEP force appears at the top position of the first electrode, which is caused by the quarter circle geometry of the first electrode (see [Fig. 1a](#)) and by the material interface between the electrode and the channel wall ([Pesch et al., 2015](#)). It is important to note that the solution is incorrect in regions very closed to the electrode edge ([Green et al., 2002](#); [Wang et al., 1996](#)), i.e., maximum value of the $\nabla|E|^2$. This numerical error, however, does not affect particles since the particle focus region is always away from the electrodes (detailed discussion see [Appendix A7](#)).

The dependence of $\nabla|E|^2$ on height was evaluated for electrodes with different spaces ([Fig. 2b](#)). Closer spaced electrodes show steeper drop of $\nabla|E|^2$ with height compared to wider spaced electrodes. The curves intersect at a height of approximately 3 mm, presenting a similar $\nabla|E|^2$ value of about $1.54 \times 10^{12} \text{ V}^2 \text{ m}^{-3}$. Below this height, 1 mm spaced electrodes show higher $\nabla|E|^2$ value

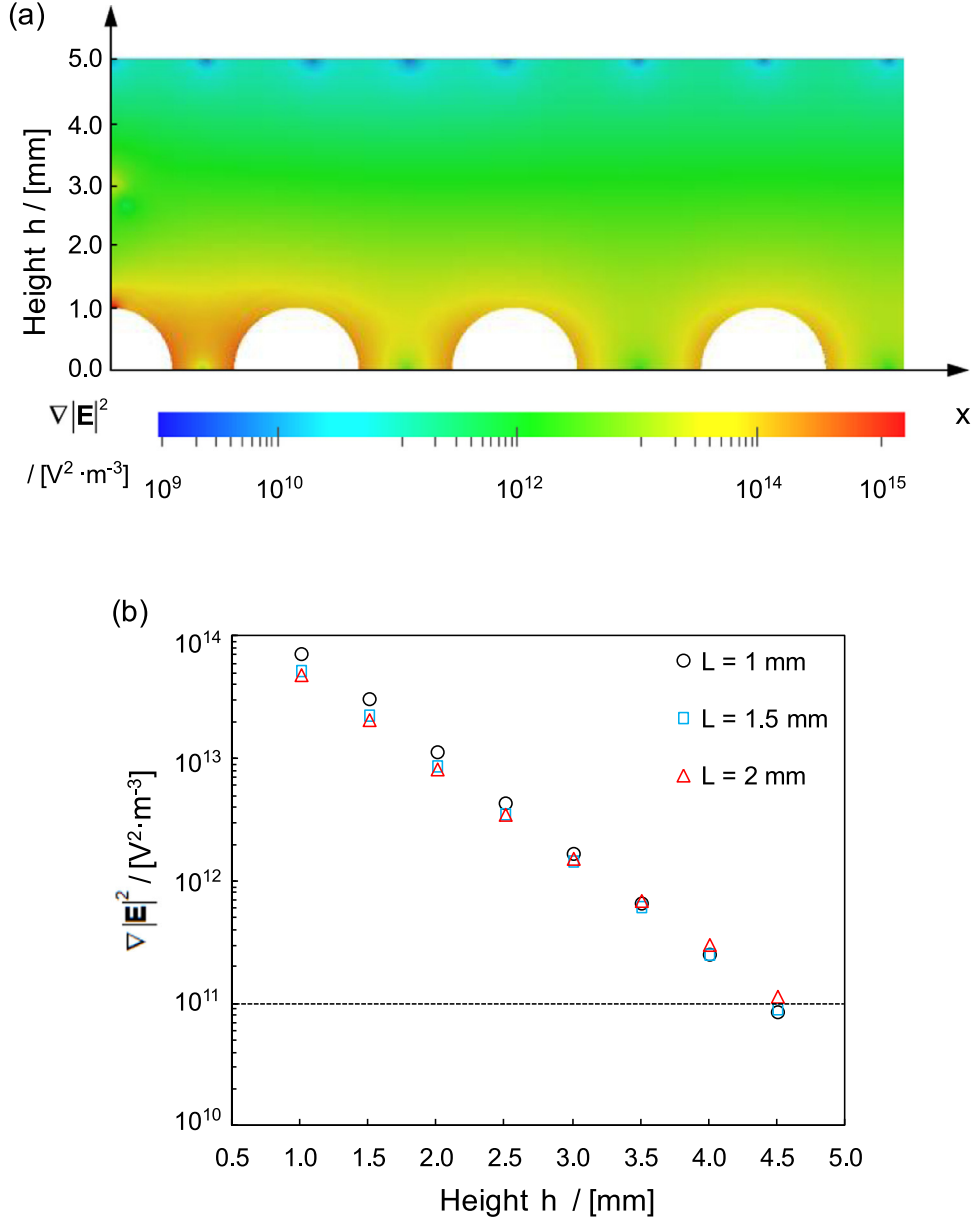


Fig. 2. (a) Calculated distribution of the gradient of square of the electric field in the initial part of the DEP channel; distances (L) between electrodes were 1 mm, 1.5 mm and 2 mm, respectively, voltage input was $200 V_{\text{eff}}$. (b) Dependence of the $\nabla|\mathbf{E}|^2$ on height for three $d=2$ mm electrode arrays with different spacing L . Dashed line indicates the $\nabla|\mathbf{E}|^2$ value at which DEP force and gravitational force are balanced.

than the other electrode spacings, and vice versa. The minimum $\nabla|\mathbf{E}|^2$ for balancing n-DEP ($Re[K]$ is specified as -0.48 at the frequency of 200 kHz) and gravitation in vertical direction in this case was calculated to be $1 \times 10^{11} \text{ V}^2 \text{ m}^{-3}$. In this particular setup, only the 2 mm spaced electrodes provide this $\nabla|\mathbf{E}|^2$ value or higher (given as dashed line in Fig. 2b) up to height of 4.5 mm (channel height 5 mm). They thus provide a larger vertical DEP working area than the other electrode spacings. The tailored electrode arrangement, i.e., increasing electrode spacing as used in the present cIDE-DEP separator, combines both a strong DEP force field at the first electrodes and a more effective DEP working area at latter electrodes.

3.2. Simulation of fluid flow and particle trajectories in the cIDE separator

The fluid flow distribution within the separator was simulated to evaluate the influence of the fluid on the particle motion. The

2.7 times higher sheath flow input rate than that of the suspension flow was optimally designed to deflect particles towards the channel bottom before they enter the separation channel (Fig. 3a). Maximum flow (red area) appears at the narrow region, in which suspension flow and sheath flow intersect into a mixed flow with a velocity of approximately 1.6 mm s^{-1} . Due to the different dimensions of the inlet channel and the separation channel, the fluid flow distribution at the interface region gives rise to a slight upward pointing flow stream at the end of the intersection area. Apart from the interface position, the flow develops homogeneously along the vertical direction of the separator.

The particles, which were injected at the top position of the suspension inlet with a specified initial velocity, were horizontally accelerated and, due to the influence of the sheath flow, perpendicularly suppressed towards the surface of the first electrode. While entering into the separation channel (yellow square in Fig. 3a), the particles were levitated significantly to different heights above the electrode. This is due to the strong negative DEP

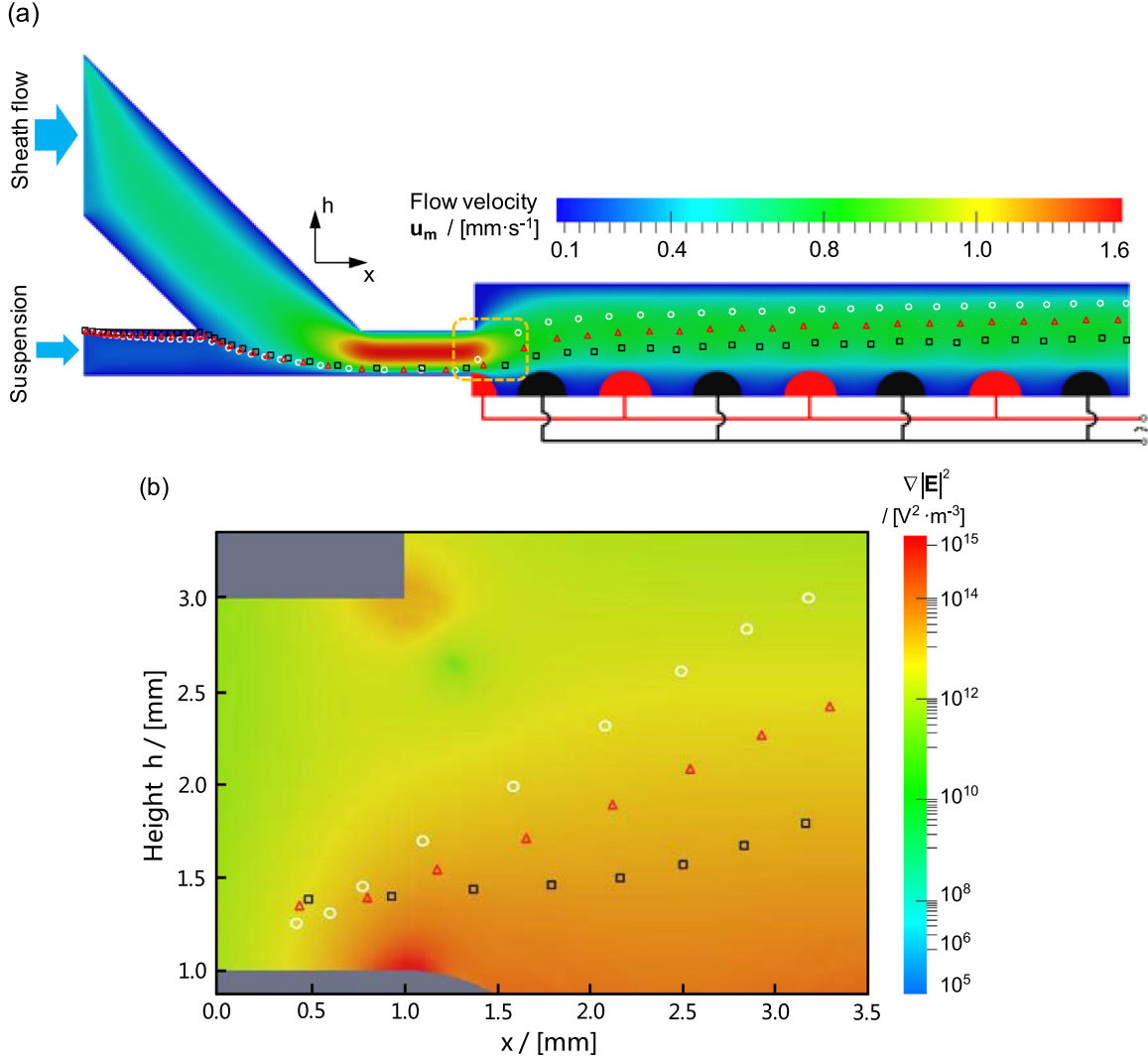


Fig. 3. (a) Simulated fluid velocity distribution and trajectories of $45\ \mu\text{m}$ (white circle), $25\ \mu\text{m}$ (red triangle) and $11\ \mu\text{m}$ (black square) PS particles ($\rho_p=1005\ \text{kg m}^{-3}$) suspended in Milli-Q[®] water ($\rho_m=1000\ \text{kg m}^{-3}$, $\mu_m=1 \times 10^{-3}\ \text{Pa s}$) in the cIDE-DEP separator. The time step between two trajectory dots is 2 s. The electric field was generated by a voltage input of $200\ V_{\text{eff}}$ at a frequency of 200 kHz. The velocity of both suspension and sheath flow at the channel inlets are 0.1 and $0.27\ \text{mm s}^{-1}$ (simulation), respectively (equivalent to 0.6 and $4.1\ \text{mL min}^{-1}$ in the experiment); (b) Particle trajectories in the entrance zone of the DEP separation channel (within the yellow square as indicated in Fig. 3a). Time step between two trajectory dots is $0.5\ \text{s}$. The background shows distribution of the $\nabla|E|^2$. (For interpretation of the references to color in this figure legend, the reader is referred to the web version of this article.)

force (Eq. (1)) acting on the polystyrene microspheres in Milli-Q water at a frequency of 200 kHz. Larger particles were repelled to higher positions than smaller particles, which is due to the cubic dependence of the DEP force on the particle radius, as described by Eq. (1), before reaching equilibrium status.

Fig. 3b shows detailed particle trajectories in the yellow square region with the $\nabla|E|^2$ distribution as background. As it can be seen, the $45\ \mu\text{m}$ particles (white circle) are repelled with the highest vertical velocity, whereas the $11\ \mu\text{m}$ (black square) particles rise up slower. The three particles gained a levitation height difference of $1.8\ \text{mm}$, $1.1\ \text{mm}$, and $0.4\ \text{mm}$ during their passage of the highlighted area. The particle levitation is fastest in the highlighted region. The following experimental validation of particle trajectories will thus focus on this region.

In the yellow square region, the DEP force reduces dramatically with particle height (particle-electrode distance) due to the small electrode spacing of $1\ \text{mm}$. The loss of DEP force is compensated thereafter by the larger spaced electrodes that provide a much larger DEP working area throughout the rest of the separation channel. As a result, although the particles rise slower after passing the first pair of electrodes, the DEP levitation continues

further in general. The effective DEP working area provided by the widely spaced electrodes levitates particles in competition with gravity in perpendicular direction (h), which results in different vertical positions h (depending on particle size) at the same horizontal position x (Fig. 3a). Simulation of particle trajectories indicate that dielectrophoretic size-based dynamic fractionation can be realized before reaching the steady state, at which all particles independent of size will have the same vertical position.

3.3. Experimental validation of particle trajectories

Experimental volumetric flows of suspension and sheath at the inlet were set to be consistent with the simulation. Both flow rate calculations were verified experimentally by measuring $11\ \mu\text{m}$ particle velocities at $x = 0$ (cf. Fig. 3b) and at different h ranging from 1 to $3\ \text{mm}$. Under the assumption of a small Stokes number, the particles will follow the fluid stream directly. This allows for measuring the fluid profile by analyzing the particle velocity as a function of h (Appendix A5). As shown in Fig. A.2, experimentally obtained particle velocities (red dots) at different heights present good agreement with the fluid profile simulation (blue line).

However, some higher particle velocity values than shown by the fluid profile were found especially at the midstream position at $h=2$ mm, which is probably attributed to the unstable sheath flow caused by the use of the peristaltic pump.

When measuring fluid flow using tracers (seed particles), the particle response time should be much smaller than the characteristic time scale of the fluid (Stokes number $Stk \ll 0.1$). The particle motion trajectories can then be used to estimate the fluid flow with sufficient accuracy (Crowe et al., 2011). The Stokes number is defined as the ratio of the particle relaxation time (τ_p) to the characteristic time of the fluid medium (τ_m), given by (Park and Jung, 2009):

$$Stk = \frac{\tau_p}{\tau_m} = \frac{2a^2\rho_p u_{max}}{9\mu_m L_c} \quad (9)$$

where u_{max} is the maximum flow velocity and L_c is the characteristic length of computational channel. The Stokes number was calculated using Eq. (9) to be 4.25×10^{-6} , meaning that the particles will follow the fluid stream almost immediately.

Trajectories of 45, 25, and 11 μm polystyrene particles were experimentally obtained by capturing the particle motion and thereafter measuring particles' x and h positions at identical time steps (0.5 s) in the highlighted region (yellow square in Fig. 3a) and the results are plotted in Fig. 4 (filled symbols) against the particle trajectories obtained by simulation (unfilled symbols). The filled symbols represent the experimental particle mean positions and the bars represent position ranges (maximum and minimum positions at each time step). Differently to the simulation, the utilization of the syringe pump for experimentally injecting particles to the suspension inlet resulted in random particle initial positions. Nearly all simulated particle positions are in good agreement with the experimental results, indicating that the model prediction of particle trajectory is reliable. For 25 μm and 11 μm particles, the experimental mean residence time is 12.5% and 25% smaller than the residence time from the simulation. This is because the unstable sheath flow, as mentioned above, gives rise to higher experimental flow rates especially at the midstream position. To our surprise, this increased flow rate in the experiments has little impact on particles' final perpendicular levitation as compared to simulation because of the extremely strong DEP force, which allows a further increase of the volume flow rate for reaching higher throughput. The increasing deviation of the

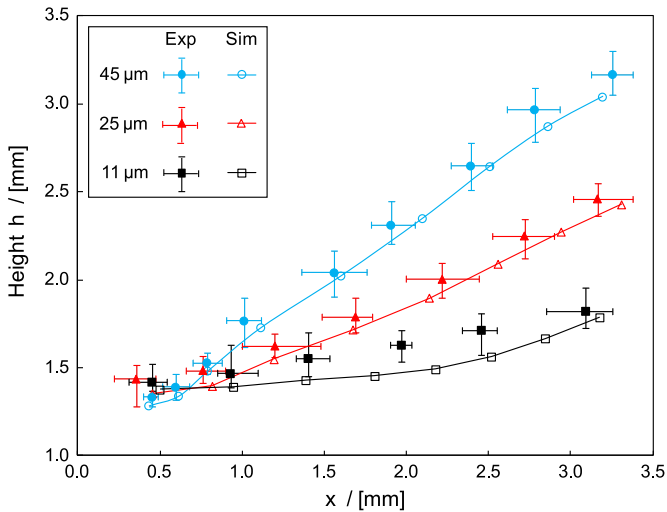


Fig. 4. Comparison of experimental and simulated results for particle trajectories. Filled symbols with position error bars represent experimental results while non-filled symbols connected with a continuous line represent simulated results. All the operation parameters are consistent with Fig. 3.

experimental particle positions towards higher values of h with decreasing particle size suggests a small deviation between the experiment and the simulated fluid flow. The fluid flow points slightly upwards after passing the constriction that will cause an upwards pointing drag force on the particles. The drag force has a quadratic dependence on the particle diameter whereas the DEP force has a cubic dependence. Hence, with decreasing particle diameter the drag force becomes more dominant over the DEP force. The deviation between the experimental fluid flow and the simulated fluid flow could, for example, be caused by the pulsed flow that is generated by the peristaltic pump.

3.4. Performance analysis of the cIDE separator

The performance of the proposed cIDE separator was quantified by introducing a dimensionless parameter, resolution of fractionation R , which is defined as the ratio of the specific target particle size, d_p^* , and the smallest size difference that can be separated, $\Delta d_p = d_{p2}^* - d_{p1}^*$ (Fig. 1d):

$$R = \frac{d_p^*}{\Delta d_p} \quad (10)$$

The definition of R is derived from Flagan (1999) for describing the performance of the differential mobility analyzer. According to Eq. (10), for a certain particle size, the resolution increases with decreasing size difference Δd_p . In the current cIDE separator, the size difference is constrained by the width of the single collector W at the channel outlet (Fig. 1d). Physically, the outlet must have a certain finite size, even if it is positioned at the correct height for a certain particle diameter. In this case, particles being a little smaller (d_{p1}^*) or bigger (d_{p2}^*) than the target particle size will also pass through the collector (Fig. 1d), which gives rise to a broad outlet particle size distribution. The resolution R is thus the ratio between target diameter and difference in separable particle size Δd_p , that is, the difference in diameter between the biggest and the smallest particle that would pass the outlet. This value depends, amongst others, on the width of the outlet. We defined it in a way that, when fractionating a certain particle size from a mixture of particle sizes, the higher the fractionation resolution, the smaller the output particle size distribution and hence the higher the purity of resultant output particles.

Fig. 5 illustrates the dependence of the resolution on collector

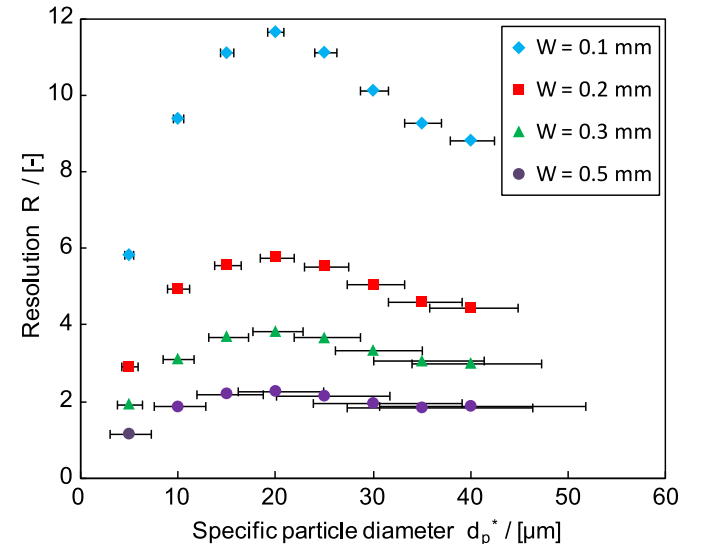


Fig. 5. Calculated separation resolution as a function of specific particle diameter and collector widths. The bars represent Δd_p . All the operating parameters are consistent with Fig. 3.

width for particles with different sizes. Each specific particle size was plotted with a bar (Δd_p) for showing the size difference. For a given collector width, the fractionation resolution R varies with the particle diameter. We believe that the first rise in the resolution can be attributed to the increasing difference in levitation speed with increasing particle size (due to the cubic dependence of the DEP force on the particle radius). A peak point appears at the specific particle diameter of around $20\ \mu\text{m}$ (Fig. 5). With increasing particle diameter above $20\ \mu\text{m}$ the resolution drops again. We believe that this is due to the fact that bigger particles reach the equilibrium faster. The drop in resolution is then because the bigger particles are already close to equilibrium and hence have only small differences in levitation height. A longer channel might be required for the fractionation of small particles to achieve better DEP levitation along the channel length, while a shorter channel might be demanded for larger particles to discriminate them before they reach the equilibrium. Consequently, the presented $20\ \mu\text{m}$ optimum particle diameter is a value specific for the given channel length (Fig. 3a) and will thus vary with varying channel geometry.

The variation tends to be more prominent at smaller collector widths, i.e. at $0.1\ \text{mm}$ it is possible to achieve much higher resolution for all particle sizes compared to other widths. Correspondingly, fine fractionation of particles with even smaller size differences can be realized with expected high resolution. On the contrary, at large widths of the collector, particle separation is only possible with huge size differences, resulting in relatively low resolutions.

Although the resolution of fractionation can be improved by narrowing the width of the collector, it is in fact not possible to separate large particles with a very small collector width, since particles would aggregate and thus clog the collector, especially at high concentrations (Moschallski et al., 2010). In addition, decreasing the collector width might cause the undesired turbulence or vortex at the channel outlet due to high Reynolds number of the fluid, which gives rise to a reduction of fractionation efficiency. Thus, a tailored outlet channel design with a collector width that is in accordance to the particle size is a key aspect for an effective fractionation. We thus evaluated the required outlet channel width as a function of the desired resolution and the outer system parameters (Fig. 6). It was found that the resultant width of the collector is strongly dependent on the operating parameters, i.e., voltage input and volume flow rate. At a given resolution, the collector width can be enlarged with increasing applied voltage, while it has to be reduced with increasing of volume flow rate (Fig. 6). Moreover, small particles are more sensitive than large particles, as they show a stronger dependence of the resultant collector width on the operation parameters (comparison of $10\ \mu\text{m}$ particles in Fig. 6a and c, to $40\ \mu\text{m}$ particles in Fig. 6b and d).

The dependence of the fractionation resolution on both operation parameters was quantitatively evaluated (Fig. 7). For a specific particle size and a given collector width, resolution increases with voltage input, while it drops with increasing volume flow rate.

In case of DEP fractionation of biological cells, it is important to note that the maximum field strength utilized in our system

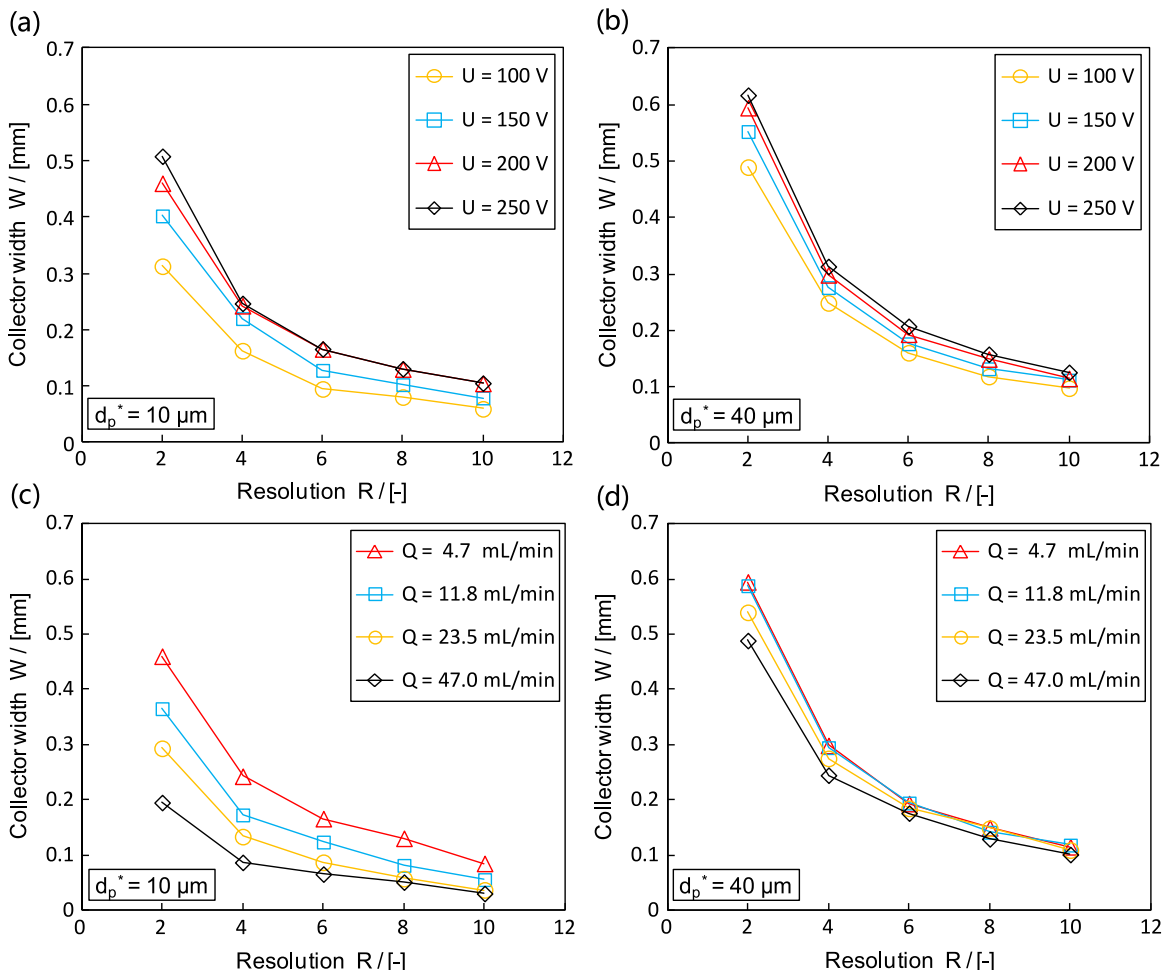


Fig. 6. Required calculated collector width W as a function of the desired resolution R for (a), (b) varied voltage input and constant volume flow rate ($4.7\ \text{mL}\ \text{min}^{-1}$) and (c), (d) varied volume flow rate and constant voltage input ($200\ \text{V}_{\text{eff}}$).

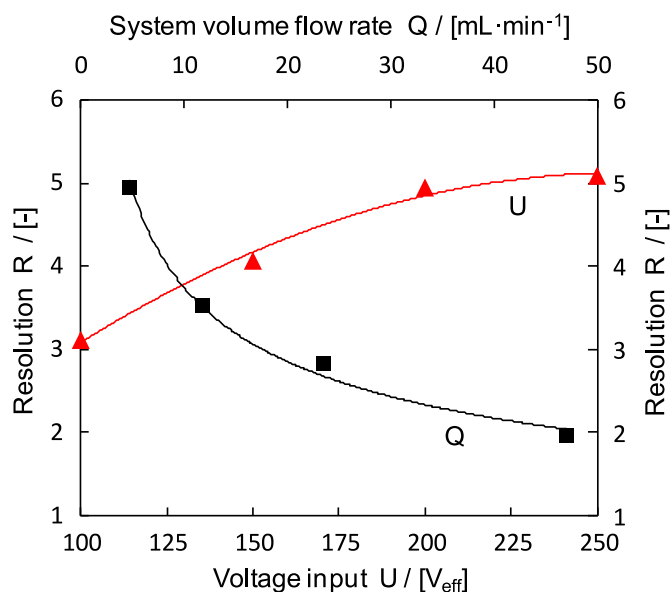


Fig. 7. Numerical estimation of the dependence of voltage input U (filled triangle with red fitting line) and system volume flow rate Q (filled square with black fitting line) on resolution R . Particles of $10\ \mu\text{m}$ in diameter were evaluated with a specified $0.2\ \text{mm}$ collector width. (For interpretation of the references to color in this figure legend, the reader is referred to the web version of this article.)

($2.5 \times 10^5\ \text{V m}^{-1}$) is nearly three times below the critical value ($7 \times 10^5\ \text{V m}^{-1}$) indicated by [Bisceglia et al. \(2015\)](#) for affecting cells' structure and induce apoptosis in cells. In addition, using an approximation given by [Voldman \(2006\)](#) the resulting imposed transmembrane potential on cells (see [Appendix A6](#)) is two orders of magnitude below its endogenous potential. Thus, very little stress is imposed on the cell membrane and hence dielectric membrane breakdown ([Heida, 2012](#)) will not happen.

To the best of our knowledge, the majority of DEP applications with respect to continuous microparticle separation were achieved with maximum system volume flow rates of up to $1\ \text{mL min}^{-1}$. The proposed cIDE-DEP separator could achieve fractionation of $10\ \mu\text{m}$ particles at a high resolution of $R=5$ (i.e., separating $10\ \mu\text{m}$ particle from $9\ \mu\text{m}$ and $11\ \mu\text{m}$ particles) and a minimum flow rate of $4.7\ \text{mL min}^{-1}$ ([Fig. 7](#)), which is a nearly fivefold increase of throughput compared to the literature. Surprisingly, a further increment of the volume flow by one order of magnitude to $47\ \text{mL min}^{-1}$ is calculated to be possible with a fractionation resolution of $R=2$, indicating that a separation of $10\ \mu\text{m}$ particle from $7.5\ \mu\text{m}$ and $12.5\ \mu\text{m}$ particles is possible ([Fig. 7](#)). In any case, it is a step towards dielectrophoretic based particle fractionation at high throughput.

4. Conclusion

In this work, a novel DEP separator with cIDE configuration was proposed for continuous microparticle fractionation at high throughput. It is based on a dielectrophoretic manipulation of particle trajectories in a flow field. The concept requires the channel to be long enough to cover the entire region in which all the particle sizes ascend towards their equilibrium state. On the other hand, depending on the target particle size and the flow rate, the channel cannot be arbitrarily long, as particles will eventually reach an equilibrium height which is identical for all particle sizes. This method can be considered as contact-free, because the electrodes, which cause the size specific levitation, repel the particles sufficiently due to the negative DEP effect and the particles do not need to be in contact with the electrodes. By tailoring the design of

the cylindrical electrode arrangement, i.e., increasing spaces between the first three electrodes, we are able to provide both a strong DEP force field at the first few electrodes and a broader DEP working area generated by the following electrodes. This allows for sustainable and effective DEP particle levitation.

Trajectories of 45 , 25 and $11\ \mu\text{m}$ particles within the cIDE-DEP separator were numerically simulated and experimentally validated with good agreement. Dielectrophoresis, having a cubic dependency on the particle radius, in combination with hydrodynamic drag and gravity was successfully used to levitate particles of different sizes to different dynamic positions. The position differences during the transient ascend of the particles allows for a size-based fractionation of particles at the outlet.

The voltage needed for size-selectively separating particle trajectories in the proposed device varied between $100\ \text{V}$ and $250\ \text{V}$ resulting in a maximum electric field strength below $2.5 \times 10^5\ \text{V m}^{-1}$. This value is nearly three times below the critical value at which the field affects the cells' structure and might induce their apoptosis. From this and the low Joule heating found (a temperature rise below $0.5\ \text{K}$) it can be concluded that the device can be used to size-selectively separate even sensitive microparticles such as living cells. However, when using media of higher conductivity, a significant temperature rise might occur that may interfere with particle trajectories inside the separator.

Further, we found that the channel used in the experiments is too long to separate the microparticles in question without increasing the flow rate by an order of magnitude. Such an increase, however, enlarges the pressure drop of the system and requires a more stable and better sealed system. The simulation, however, demonstrates the possibility of fractionation clearly.

With respect to device performance, a dimensionless parameter, resolution, is introduced for quantitative characterization of the fractionation accuracy. Numerical predictions show that the resolution increases with decreasing collector width at the outlet channel. For a given target resolution, the required collector width increases with voltage and decreases with volume flow rate. At a specified width of the collector, a high resolution can be achieved by trading-off voltage and volume flow rate. The results indicate the possibility of continuous dielectrophoretic microparticle fractionation with high resolution and at high throughput.

Acknowledgements

The authors wish to acknowledge German Research Foundation (DFG) for financial support (TH 893/9-1). Yan Wang would like to thank China Scholarship Committee (CSC) for financially supporting his contribution (CSC [2011] 3005). Georg R. Pesch would like to thank the DFG for financial support within the research training group "Micro-, meso- and macroporous nonmetallic Materials: Fundamentals and Applications" (GRK 1860).

Appendix A. Supplementary material

Supplementary data associated with this article can be found in the online version at <http://dx.doi.org/10.1016/j.ces.2016.07.020>.

References

- Baune, M., Du, F., Thöming, J., 2008. Dielectrophoresis—bridging the scale in modeling and application. *Vernetzte Wissenschaften*, Logos Verlag Berlin GmbH, Berlin, pp. 47–64.
- Bettelheim, F., Brown, W., Campbell, M., Farrell, S., Torres, O., 2012. *Introduction to General, Organic and Biochemistry*. Cengage Learning, Brooks/Cole, 10 Davis Drive, Belmont, CA 94002-3098, USA.

- Bisceglia, E., Cubizolles, M., Trainito, C.I., Berthier, J., Pudda, C., François, O., Mallard, F., Le Piouffe, B., 2015. A generic and label free method based on dielectrophoresis for the continuous separation of microorganism from whole blood samples. *Sens. Actuators B: Chem.* 212, 335–343.
- Cao, J., Cheng, P., Hong, F., 2008. A numerical analysis of forces imposed on particles in conventional dielectrophoresis in microchannels with interdigitated electrodes. *J. Electrostat.* 66 (11), 620–626.
- Castellanos, A., Ramos, A., Gonzalez, A., Green, N.G., Morgan, H., 2003. Electrohydrodynamics and dielectrophoresis in microsystems: scaling laws. *J. Phys. D: Appl. Phys.* 36 (20), 2584.
- Čemažar, J., Douglas, T.A., Schmelz, E.M., Davalos, R.V., 2016. Enhanced contactless dielectrophoresis enrichment and isolation platform via cell-scale microstructures. *Biomicrofluidics* 10 (1), 014109.
- Çetin, B., Kang, Y., Wu, Z., Li, D., 2009. Continuous particle separation by size via AC-dielectrophoresis using a lab-on-a-chip device with 3–D electrodes. *Electrophoresis* 30 (5), 766–772.
- Çetin, B., Li, D., 2011. Dielectrophoresis in microfluidics technology. *Electrophoresis* 32 (18), 2410–2427.
- Cheng, I.-F., Froude, V.E., Zhu, Y., Chang, H.-C., Chang, H.-C., 2009. A continuous high-throughput bioparticle sorter based on 3D traveling-wave dielectrophoresis. *Lab Chip* 9 (22), 3193–3201.
- Chuang, H.-S., Chung, T.-Y., Li, Y., 2014. Compact and tunable size-based dielectrophoretic flow fractionation. *J. Micromech. Microeng.* 24 (12), 125016.
- Crews, N., Darabi, J., Voglewede, P., Guo, F., Bayoumi, A., 2007. An analysis of interdigitated electrode geometry for dielectrophoretic particle transport in microfluidics. *Sens. Actuators B: Chem.* 125 (2), 672–679.
- Crowe, C.T., Schwarzkopf, J.D., Sommerfeld, M., Tsuji, Y., 2011. *Multiphase Flows with Droplets and Particles*. CRC Press, 6000 Broken Sound Parkway NW, Suite 300, Boca Raton, FL 33487-2742, USA.
- Doh, I., Cho, Y.-H., 2005. A continuous cell separation chip using hydrodynamic dielectrophoresis (DEP) process. *Sens. Actuators A: Phys.* 121 (1), 59–65.
- Du, F., Baune, M., Kück, A., Thöming, J., 2008. Dielectrophoretic gold particle separation. *Sep. Sci. Technol.* 43 (15), 3842–3855.
- Du, F., Baune, M., Thöming, J., 2007. Insulator-based dielectrophoresis in viscous media—simulation of particle and droplet velocity. *J. Electrostat.* 65 (7), 452–458.
- Ermolina, I., Morgan, H., 2005. The electrokinetic properties of latex particles: comparison of electrophoresis and dielectrophoresis. *J. Colloid Interface Sci.* 285 (1), 419–428.
- Fedotov, P.S., Vanifatova, N.G., Shkinev, V.M., Spivakov, B.Y., 2011. Fractionation and characterization of nano- and microparticles in liquid media. *Anal. Bioanal. Chem.* 400 (6), 1787–1804.
- Flagan, R.C., 1999. On differential mobility analyzer resolution. *Aerosol Sci. Technol.* 30 (6), 556–570.
- Fukuda, S., Schmid-Schönbein, G.W., 2002. Centrifugation attenuates the fluid shear response of circulating leukocytes. *J. Leukoc. Biol.* 72 (1), 133–139.
- Gadish, N., Voldman, J., 2006. High-throughput positive-dielectrophoretic bioparticle microconcentrator. *Anal. Chem.* 78 (22), 7870–7876.
- Green, N.G., Ramos, A., Morgan, H., 2002. Numerical solution of the dielectrophoretic and travelling wave forces for interdigitated electrode arrays using the finite element method. *J. Electrostat.* 56 (2), 235–254.
- Han, C., Sun, J., Liu, J., Cheng, H., Wang, Y., 2015. A pressure-driven capillary electrophoretic system with injection valve sampling. *Analyst* 140 (1), 162–173.
- Han, K.-H., Han, S.-I., Frazier, A.B., 2009. Lateral displacement as a function of particle size using a piecewise curved planar interdigitated electrode array. *Lab Chip* 9 (20), 2958–2964.
- Heida, T., 2012. *Electric Field-induced Effects on Neuronal Cell Biology Accompanying Dielectrophoretic Trapping*. 173. Springer Science & Business Media, Tiergartenstrasse 17, D-69121 Heidelberg, Germany.
- Huang, Y., Wang, X.-B., Becker, F.F., Gascoyne, P., 1997. Introducing dielectrophoresis as a new force field for field-flow fractionation. *Biophys. J.* 73 (2), 1118–1129.
- Jin, C., McFaul, S.M., Duffy, S.P., Deng, X., Tavassoli, P., Black, P.C., Ma, H., 2014. Technologies for label-free separation of circulating tumor cells: from historical foundations to recent developments. *Lab Chip* 14 (1), 32–44.
- Jones, T., 1995. *Electromechanics of Particles*. Cambridge, Cambridge.
- Kang, K.H., Kang, Y., Xuan, X., Li, D., 2006. Continuous separation of microparticles by size with direct current-dielectrophoresis. *Electrophoresis* 27 (3), 694–702.
- Kang, Y., Cetin, B., Wu, Z., Li, D., 2009. Continuous particle separation with localized AC-dielectrophoresis using embedded electrodes and an insulating hurdle. *Electrochim. Acta* 54 (6), 1715–1720.
- Katasonova, O., Fedotov, P., 2009. Methods for continuous flow fractionation of microparticles: outlooks and fields of application. *J. Anal. Chem.* 64 (3), 212–225.
- Khoshmanesh, K., Nahavandi, S., Baratchi, S., Mitchell, A., Kalantar-zadeh, K., 2011. Dielectrophoretic platforms for bio-microfluidic systems. *Biosens. Bioelectron.* 26 (5), 1800–1814.
- Kissa, E., 1999. *Dispersions: Characterization, Testing, and Measurement*. CRC Press, 270 Madison Avenue, New York, NY 10016, USA, p. 84.
- Kralj, J.G., Lis, M.T., Schmidt, M.A., Jensen, K.F., 2006. Continuous dielectrophoretic size-based particle sorting. *Anal. Chem.* 78 (14), 5019–5025.
- Kuntaegowdanahalli, S.S., Bhagat, A.A.S., Kumar, G., Papautsky, I., 2009. Inertial microfluidics for continuous particle separation in spiral microchannels. *Lab Chip* 9 (20), 2973–2980.
- Leal, L.G., 2007. *Advanced Transport Phenomena: Fluid Mechanics and Convective Transport Processes*. Cambridge University Press, Complexe Futur X, Bld Industriel 58 E28, 7700 Mouscron, Belgium.
- Lee, D., Kim, D., Kim, Y., Park, K.-h., Oh, E.-J., Kim, Y., Kim, B., 2013. A negative dielectrophoresis and gravity-driven flow-based high-throughput and high-efficiency cell-sorting system. *J. Lab. Autom.*, 2211068213498385
- Lenhof, A., Laurell, T., 2010. Continuous separation of cells and particles in microfluidic systems. *Chem. Soc. Rev.* 39 (3), 1203–1217.
- Leu, T.-S., Weng, C.-Y., 2009. Studies of particle levitation in a dielectrophoretic field-flow fractionation-based microsorter. *J. Micro/Nanolithography MEMS MOEMS* 8 (2), 021106-021106-5.
- Lewpiriyawong, N., Yang, C., Lam, Y.C., 2010. Continuous sorting and separation of microparticles by size using AC dielectrophoresis in a PDMS microfluidic device with 3–D conducting PDMS composite electrodes. *Electrophoresis* 31 (15), 2622–2631.
- Li, X., Chin, E., Sun, H., Kurup, P., Gu, Z., 2010. Fabrication and integration of metal oxide nanowire sensors using dielectrophoretic assembly and improved post-assembly processing. *Sens. Actuators B: Chem.* 148 (2), 404–412.
- Li, Y., Dalton, C., Crabtree, H.J., Nilsson, G., Kaler, K.V., 2007. Continuous dielectrophoretic cell separation microfluidic device. *Lab Chip* 7 (2), 239–248.
- Ling, S.H., Lam, Y.C., Chian, K.S., 2012. Continuous cell separation using dielectrophoresis through asymmetric and periodic microelectrode array. *Anal. Chem.* 84 (15), 6463–6470.
- Markx, G.H., Pethig, R., Rousselet, J., 1997. The dielectrophoretic levitation of latex beads, with reference to field-flow fractionation. *J. Phys. D: Appl. Phys.* 30 (17), 2470.
- Markx, G.H., Talary, M.S., Pethig, R., 1994. Separation of viable and non-viable yeast using dielectrophoresis. *J. Biotechnol.* 32 (1), 29–37.
- Mathew, B., Alazzam, A., Abutayeh, M., Gawanmeh, A., Khashan, S., 2015. Modeling the trajectory of microparticles subjected to dielectrophoresis in a microfluidic device for field flow fractionation. *Chem. Eng. Sci.* 138, 266–280.
- Messaud, F.A., Sanderson, R.D., Runyon, J.R., Otte, T., Pasch, H., Williams, S.K.R., 2009. An overview on field-flow fractionation techniques and their applications in the separation and characterization of polymers. *Prog. Polym. Sci.* 34 (4), 351–368.
- Moon, H.-S., Kwon, K., Kim, S.-I., Han, H., Sohn, J., Lee, S., Jung, H.-I., 2011. Continuous separation of breast cancer cells from blood samples using multi-orifice flow fractionation (MOFF) and dielectrophoresis (DEP). *Lab Chip* 11 (6), 1118–1125.
- Morgan, H., Green, N.G., 2003. *AC Electrokinetics: Colloids and Nanoparticles*. Research Studies Press, Baldock, Hertfordshire, England.
- Moschallski, M., Hausmann, M., Posch, A., Paulus, A., Kunz, N., Duong, T.T., Angres, B., Fuchsberger, K., Steuer, H., Stoll, D., 2010. MicroPrep: Chip-based dielectrophoretic purification of mitochondria. *Electrophoresis* 31 (15), 2655–2663.
- Niil, H., Sun, T., Green, N., 2011. Higher order dielectrophoretic force characterisation of non-spherical particles. *J. Phys. Conf. Ser.*, 012061.
- Park, J.-S., Jung, H.-I., 2009. Multiorifice flow fractionation: continuous size-based separation of microspheres using a series of contraction/expansion microchannels. *Anal. Chem.* 81 (20), 8280–8288.
- Pesch, G.R., Du, F., Schwientek, U., Gehrmeier, C., Maurer, A., Thöming, J., Baune, M., 2014. Recovery of submicron particles using high-throughput dielectrophoretically switchable filtration. *Sep. Purif. Technol.* 132, 728–735.
- Pesch, G.R., Kiewidit, L., Du, F., Baune, M., Thöming, J., 2015. Electrodeless Dielectrophoresis: Impact of geometry and material on obstacle polarization. *Electrophoresis*.
- Pethig, R., 2010. Review article—dielectrophoresis: status of the theory, technology, and applications. *Biomicrofluidics* 4 (2), 022811.
- Pethig, R., 2013. Dielectrophoresis: an assessment of its potential to aid the research and practice of drug discovery and delivery. *Adv. drug Deliv. Rev.* 65 (11), 1589–1599.
- Pohl, H.A., 1978. *Dielectrophoresis: The Behavior of Neutral Matter in Nonuniform Electric Fields*. Cambridge University Press, Cambridge, p. 80.
- Qian, C., Huang, H., Chen, L., Li, X., Ge, Z., Chen, T., Yang, Z., Sun, L., 2014. Dielectrophoresis for bioparticle manipulation. *Int. J. Mol. Sci.* 15 (10), 18281–18309.
- Ramos, A., Morgan, H., Green, N.G., Castellanos, A., 1998. AC electrokinetics: a review of forces in microelectrode structures. *J. Phys. D: Appl. Phys.* 31 (18), 2338.
- Seminario, L., Rozas, R., Bórquez, R., Toledo, P.G., 2002. Pore blocking and permeability reduction in cross-flow microfiltration. *J. Membr. Sci.* 209 (1), 121–142.
- Song, S., Choi, S., 2013. Design rules for size-based cell sorting and sheathless cell focusing by hydrophoresis. *J. Chromatogr. A* 1302, 191–196.
- Voldman, J., 2006. Electrical forces for microscale cell manipulation. *Annu. Rev. Biomed. Eng.* 8, 425–454.
- Wang, X.-B., Vykoukal, J., Becker, F.F., Gascoyne, P.R., 1998. Separation of polystyrene microbeads using dielectrophoretic/gravitational field-flow-fractionation. *Biophys. J.* 74 (5), 2689–2701.
- Wang, X., Wang, X.-B., Becker, F., Gascoyne, P.R., 1996. A theoretical method of electrical field analysis for dielectrophoretic electrode arrays using Green's theorem. *J. Phys. D: Appl. Phys.* 29 (6), 1649.
- Wang, Y., Du, F., Baune, M., Thöming, J., 2014. Dielectrophoresis in aqueous suspension: impact of electrode configuration. *Microfluid. nanofluidics* 17 (3), 499–507.
- Wang, Y., Du, F., Baune, M., Thöming, J., 2015. Predicting and eliminating Joule heating constraints in large dielectrophoretic IDE separators. *Chem. Eng. Sci.* 137, 235–242.
- Wood, N.R., Wolsiefer, A.I., Cohn, R.W., Williams, S.J., 2013. Dielectrophoretic trapping of nanoparticles with an electrokinetic nanoprobe. *Electrophoresis* 34 (13), 1922–1930.
- Xie, Y., Zheng, D., Li, Q., Chen, Y., Lei, H., Pu, L.L., 2010. The effect of centrifugation on viability of fat grafts: an evaluation with the glucose transport test. *J. Plast. Reconstr. Aesthet. Surg.* 63 (3), 482–487.
- Xu, R., 2001. *Particle Characterization: Light Scattering Methods*. 13. Springer Science & Business Media, P.O. Box 17, 3300 AA Dordrecht, the Netherlands.
- Yamada, M., Nakashima, M., Seki, M., 2004. Pinched flow fractionation: continuous size separation of particles utilizing a laminar flow profile in a pinched microchannel. *Anal. Chem.* 76 (18), 5465–5471.
- Zhang, J., Yan, S., Sluyter, R., Li, W., Alici, G., Nguyen, N.-T., 2014. Inertial particle separation by differential equilibrium positions in a symmetrical serpentine micro-channel. *Sci. Rep.*, 4.